REPORT DOCUMENTATION PAGE

1. REPORT DATE *(DD-MM-YYYY)*	2. REPORT TYPE Technical Paper	3. DATES COVERED *(From - To)*

4. TITLE AND SUBTITLE

Please see attached

5a. CONTRACT NUMBER

5b. GRANT NUMBER

5c. PROGRAM ELEMENT NUMBER

6. AUTHOR(S)

5d. PROJECT NUMBER
2308

5e. TASK NUMBER
M13C

5f. WORK UNIT NUMBER
346057

7. PERFORMING ORGANIZATION NAME(S) AND ADDRESS(ES)

ERC

8. PERFORMING ORGANIZATION REPORT

9. SPONSORING / MONITORING AGENCY NAME(S) AND ADDRESS(ES)

Air Force Research Laboratory (AFMC)
AFRL/PRS
5 Pollux Drive
Edwards AFB CA 93524-7048

10. SPONSOR/MONITOR'S ACRONYM(S)

11. SPONSOR/MONITOR'S NUMBER(S)

Please see attached

12. DISTRIBUTION / AVAILABILITY STATEMENT

Approved for public release; distribution unlimited.

13. SUPPLEMENTARY NOTES

14. ABSTRACT

20030116 054

15. SUBJECT TERMS

16. SECURITY CLASSIFICATION OF:			17. LIMITATION OF ABSTRACT	18. NUMBER OF PAGES	19a. NAME OF RESPONSIBLE PERSON Leilani Richardson
a. REPORT Unclassified	b. ABSTRACT Unclassified	c. THIS PAGE Unclassified	A		19b. TELEPHONE NUMBER *(include area code)* (661) 275-5015

✓ Spreadsheet
✓ OTS

MEMORANDUM FOR IN-HOUSE PUBLICATIONS

FROM: PROI (TI) (STINFO)   20 Nov 98

SUBJECT: Authorization for Release of Technical Information, Control Number: AFRL-PR-ED-TP-FY99-0024
<u>Chehroudi (HSTX),Talley, Coy, "Initial Growth Rate and Visual Characteristics of a Round Jet into a Sub- to
Supercritical Environment of Relevance to Rocket, Gas Turbine, and Diesel Engines"</u>

37th AIAA Aerospace Sciences Meeting   (Statement A)
also submission to AIAA Journal of Propulsion and Power

AIAA 99-0206
Initial Growth Rate and Visual Characteristics of a Round Jet into a Sub- to Supercritical Environment of Relevance to Rocket, Gas Turbine, and Diesel Engines

B. Chehroudi[*], D. Talley, and E. Coy

Air Force Research Laboratory
10 E. Saturn Boulevard
Edwards AFB, CA 93524-7680

0

Initial Growth Rate and Visual Characteristics of a Round Jet into a Sub- to Supercritical Environment of Relevance to Rocket, Gas Turbine, and Diesel Engines

B. Chehroudi[*], D. Talley, and E. Coy

Air Force Research Laboratory; AFRL/PRSA
10 E. Saturn Boulevard
Edwards AFB, CA 93524-7680

Abstract

The combustion chamber temperature and pressure in many liquid rocket, gas turbine, and diesel engines are quite high and can reach above the critical point of the injected fuels and/or oxidizers. A high pressure chamber is used to investigate and understand the nature of the interaction between the injected fluid and the environment under such conditions. Pure N_2, He, and O_2 fluids are injected. Several chamber media are selected including, N_2, He, and mixtures of $CO+N_2$. The effects of chamber pressure ranging from a subcritical (i.e. relative pressure, $P_r = P/P_{injectant\ critical} < 1$) to a supercritical ($P_r > 1$) value at a supercritical chamber temperature (i.e. relative temperature $T_r = T/T_{injectant\ critical} > 1$) are photographically observed and documented near the injector hole exit region using a CCD camera illuminated by a short-duration back-lit strobe light. At low subcritical chamber pressures, the jets exhibit surface irregularities that amplify downstream, looking intact, shiny, but wavy (sinuous) on the surface that eventually break up into irregularly-shaped small entities. A further increase of chamber pressure causes formation of many small droplets on the surface of the jet ejecting away only within a narrow region below the critical pressure of the injected fluid similar to a second wind-induced liquid jet breakup regime. Raising the chamber pressure, transition into a full atomization regime is inhibited by reaching near, but slightly lower than, the critical pressure of the injectant where both surface tension and heat of vaporization are sufficiently reduced. The jet appearance changes abruptly at this point and remains the same to resemble a turbulent gas jet injection. In this region, and within the imaging resolution limitation, no droplets are seen forming and/or departing from the jet. The jet initial total divergence angle, indicating initial growth or spreading rate, is extracted from a large set of images and plotted along with the available data on liquid fuel injection in a diesel engine environment, turbulent incompressible, supersonic, and variable-density jets and mixing layers, creating a unique plot on its own. The jet spreading rate measurements agree well with a theoretical equation proposed by *Papamoschou and Roshko [1]* and closely follow the trend of that of *Dimotakis [2]* for incompressible but variable-density turbulent mixing layers, thus quantitatively strengthening the gas-jet like appearance. Considering this agreement, the inhibition of the transition to atomization regime and its confirmation through the examined atomization criteria, and the visual lack of any drop; the relevancy of current injection models and some drop vaporization/combustion results under conditions where gas-jet like appearance is observed should be reexamined.

Introduction

In many power production machines liquid fuel is injected into a high temperature and pressure combustion chamber to react with an oxidizer and release of the fuel's chemical energy. Such relevant examples are rocket, gas turbine, and diesel engines. In the designs of chemical rocket engines liquid fuel and oxidizer are injected through openings to form round jets, coaxial or impinging types, entering into the hot and elevated pressure environment of the combustion chamber. Simple thermodynamic analysis of the rocket thrust chamber (combustion chamber plus the expansion nozzle) shows that, for a given thrust, the rocket size may be decreased as chamber pressure is increased. The extent of this benefit, however, is lowered by other considerations such as higher thrust chamber stresses, heat transfer rates, and pump power and size. As far as the combustion is concerned, effects of increased chamber pressure are to decrease dissociation of the molecules and hence increase the effective heat release. Higher effective heat release, theoretically, delivers higher specific impulse. Hence motivation towards higher chamber pressures are justified. In diesel engines, the higher the compression ratio the higher the thermal efficiency, being the desired trend. In addition, extremely high in-cylinder liquid fuel injection pressures of up to 200 MPa are employed for better air/fuel mixing to reduce soot formation and EPA-regulated exhaust smoke. In gas turbine engines, high compressor pressure ratios (translate into high chamber

pressures) and elevated combustor exit temperatures lead to better thermal efficiencies.

In all of the above examples, due to the high pressure trends and existence of high temperature in the combustor, injected liquid may find itself near or even above the thermodynamic critical condition. For example, the Space Shuttle main engine thrust chamber pressure is about 22.3 MPa. And, the combustion chamber pressure for Vulcain (Ariane 5) with liquid H_2/liquid O_2 can reach up to 10 MPa while a record pressure of nearly 28.2 MPa has been reported. Very little information is available on liquid jets injected into supercritical condition. And this leads to our motivation in initiating an organized and systematic experimental effort investigating liquid jets under sub- and supercritical conditions.

There are drastic changes in some important properties of a pure substance as it approaches the thermodynamic critical point (CP). For example, under thermodynamic equilibrium condition, the distinction between liquid and gas phases disappears at and above the critical point and it is simply referred to as "fluid". This phenomenon was first discovered in 1821 by Baron Charles Cagniard dela Tour, a French scientist, who heard no splashing of the mixture of liquid and gas above a certain temperature. Also, large changes in density occur near the critical point. Other properties that change widely near the critical point are thermal conductivity, mass diffusivity, and surface tension. Indeed, constant-pressure specific heat values become very large and surface tension vanishes at the critical point. For these reasons most applications avoid operation near the critical point. In many practical applications liquid fuel is vaporized or burned in an environment consisting of air and/or products of combustion. Also, as ambient pressure is raised the importance of solubility of gases into the liquid phase increases and one should consider multicomponent phase equilibrium information. For mixtures, determination of the critical conditions, called "critical mixing temperature or pressure" (critical lines for a two-component mixture as opposed to a critical point for a pure substance), are complex, see *Bruno and Ely [3]*. For example, for a pure hydrocarbon drop in a nitrogen environment, the amount of nitrogen dissolved on the surface of the liquid drop increases with pressure and, in addition, critical mixing temperature declines, see *Lazar and Faeth [4]*. Therefore, although a pure liquid fuel drop is introduced, a thin layer, due to low liquid mass diffusivity neglecting internal flows, on its surface is a mixture of nitrogen and the fuel that spreads spatially in time, see *Umemura [5]*. In what follows, unless otherwise made clear, the terms subcritical and supercritical, and relative pressure and temperature are referenced with respect to the critical condition of the pure substance used in drops or jets and not the environment.

Prior to introduction to liquid jet injection into sub- to supercritical condition it is informative to briefly review important findings of liquid droplet vaporization and combustion at high pressure conditions in this and the next paragraphs. The justification is that some physical phenomena observed in these studies may be of use for jet injection. After all, the expectation is that upon injection a jet is atomized into droplets that are then exposed to these conditions. There are many experimental and computer modeling works on droplet vaporization and combustion at elevated pressures. In summary, for nonreacting case, when a drop of a pure substance is exposed to an environment of a different pure substance at $T_r > 1$ but at P_r less than some value ($P_r = P_t$; P_t near 2), drop temperature increases up to a pseudo-wet bulb temperature and settles there until full evaporation. At the wet-bulb condition, all of the heat added to the drop is for the latent heat of vaporization and there is no drop heat up. As environment pressure is increased, in a transition region, $P_t < P_r < P_m$, the pseudo-wet bulb temperature approaches the mixture critical temperature, the drop surface temperature reaches the critical mixing temperature sometime during its life time (for example, at P_t it occurs at the end of its lifetime), and the enthalpy of vaporization vanishes. Above the P_m, drop temperature monotonically increases and rapidly reaches the critical mixing temperature before its lifetime. There is no pseudo-wet bulb temperature in this case. Due to the increased solubility at high pressure, the drop (particularly a thin layer near the surface neglecting drop internal flow) reaches the critical mixing temperature, distinction between phases is then lost and, for surface regression rate analysis, the movement of the "front" at critical mixing temperature is tracked in computational efforts. The center of the drop is believed to be in liquid phase until the critical mixing temperature "front" is arrived. Generally, for hydrocarbons in nitrogen environment and at any fixed relative ambient temperature of up to about 2, the drop gasification lifetime increases with ambient pressure and levels off (or starts to decrease mildly) at about (1 to 3)*$P_{critical}$ depending on T_r. Above T_r of 2, gasification lifetime drops sharply with pressure, *see Giveler and Abraham [6]*, to a minimum at about P_r of 5, *see Umemura [5]*, and rises again due to lowered mass diffusivity at high pressures. Initial decline in gasification time with pressure is primarily due to reduced enthalpy of vaporization but later when it vanishes, low mass diffusivities slow down the gasification process.

For the combustion of drops, the flame envelope creates another source of heat addition after ignition and also acts as a sink for the vaporized and diffused fuel and oxidizer molecules. Pioneering drop combustion experiments by *Faeth et al. [7]* in lowered gravity condition show that at low pressures, pure fuel drop temperature, measured inside of it via a thermocouple bead junction, rises to a plateau at wet-bulb temperature, being near the boiling temperature at pressures below the critical pressure of drop. After the end of this plateau period, also called quasi-steady-state-behavior period, where gasification is completed, the measured temperature rises again until the end of the combustion. This whole picture repeats itself up to about two and a

half the critical pressure of the fuel beyond which no wet-bubble plateau is observed. *Faeth et al. [7]* define this condition as the onset of the supercritical burning. Beyond this ambient pressure, drop temperature increases monotonically until the complete burnout. It is also found that the combustion time (i.e., from ignition to when all fuel is burned) decreases to a local minimum near the fuel's critical pressure and then increases, whereas gasification time (i.e., from when drop is exposed to ambient to when all fuel is gasified) continuously shortens. Computational modeling work by *Shuen et al. [8]* reveals detailed information on a liquid drop combustion under sub- and supercritical conditions. According to them, as ambient pressure is raised, ambient-gas solubility in the liquid phase increases causing lowered critical mixing temperature until eventually the time-increasing surface temperature reaches this critical mixing value at which time latent heat of vaporization vanishes. Computed trends of combustion lifetime with ambient pressure for large drops (1000 micron) behave similar to the experimental observations of *Faeth et al. [7]*. Similar results for small drops do not show this trend and combustion time increases monotonically. *Shuen et al. [8]* also show that flame radiation can play an important role for large drops and must be accounted for in modeling efforts. There are two other interesting results. First, time histories of the fuel mass, as opposed to surface regression rate, indicate that gasification is facilitated more at high pressures. Second, flame temperature continuously decreases with ambient pressure for large drops due to importance of lowered mass diffusivity at high pressures and also, for the same conditions, flame temperature is higher for small drops. These two results suggest higher ambient pressures and better liquid fuel atomization for rocket, gas turbine, and diesel engines.

There are a few works on liquid injection into supercritical condition, notably *Newman and Brzustowski [9]* and *Mayer et al.[10], [11]* at high Reynolds numbers and *Woodward and Talley [12]* at low Reynolds numbers. *Newman and Brzustowski [9]* use steady CO_2 jet injected into a chamber of pure N_2 and mixtures of CO_2+N_2 at both sub- and supercritical pressures and temperatures. Note that if chamber is at supercritical pressure the injected jet pressure is higher and must also be supercritical. At just above critical pressure of CO_2, injection of CO_2 into mixtures of CO_2+N_2, varying initial CO_2 concentration to change mixture density, shows thickening and widening of the jet due to changes in chamber-to-injectant density ratio. At a high supercritical pressure, injection of CO_2 into a pure varying sub- to supercritical temperature N_2 causes shortening of both the jet length and its width with chamber temperature. They explain effects of increased chamber temperature on jet appearance to be due to progressive reduction in ambient gas density, lowering in surface tension to zero at critical temperature, and increase in liquid CO_2 evaporation. *Newman and Brzustowski [9]*, in experiments where CO_2 is injected into a mixture of CO_2+N_2 with constant but large initial

CO_2 mass fraction (to reduce jet evaporation) at a fixed supercritical temperature but varying sub- to supercritical pressures, propose possibility of gasification and that at supercritical temperatures and pressures the jet can be considered as a variable-density single-phase turbulent submerged gas jet. Finally, assuming self-preserving flow, negligible gravity, zero latent heat of vaporization, ideal gas behavior, and thermal equilibrium between gas and drops, they develop a model for predicting the profile of the outer extent of a supercritical steady jet and its centerline mean axial velocity. Comparison with experiment was poor near the injector. *Mayer et al [11]* use liquid N_2 (LN_2) jet at 105 K into a N_2 environment at 300 K but at varying ambient pressures ranging from sub- to supercritical conditions and observe drastic changes in the jet structure near and above the critical pressure. The jet behaves similar to the classical atomization of liquid fuel with ligaments and drops near the critical pressure. They attribute this behavior to a continual decline of surface tension until it vanishes at and beyond critical point. They also consider He(at 280 K) and N_2(at 97 K) combination injection, as simulant fluids for H_2 and O_2 combination, through a coaxial injector (N_2 in the center hole, He through the outer annular space) similar to the ones used in the cryogenic rocket engines. Again, changes in the jet structure at high pressures as solubility of He into N_2 increases and surface tension reduces are clear. For example, at each fixed pressure above the critical pressure of oxygen, for a binary mixture of H_2+O_2, surface tension declines with temperature to a zero value at the critical mixing temperature. They also observe jet structural changes in both ignition and combustion phases of the H_2 and O_2 system in a model of a rocket combustion chamber. They report no evidence of droplets at supercritical combustion. For an N_2-into-N_2 cryogenic jet, *Woodward and Talley [12]* showed that the addition of He gas to the supercritical ambient N_2 fluid forced the jet to look like injection into the subcritical ambient condition.

In what follows experimental arrangement is described followed by presentation of results and their discussion under jet structure and jet spreading angle. The paper concludes with summary and conclusion section.

Experimental setup

Figure 1 shows schematic drawing of the experimental set up. It consists of three main sections: high pressure chamber, cryogenic cooler, and plumbing for introduction of different substances as ambient media inside the chamber and for routing of the injectants through the injector. The high pressure chamber is constructed with stainless steel to withstand pressures and temperatures of up to 137 atm (2000 psi) and 473 K, respectively. For optical diagnostics, there are provisions for two facing circular sapphire windows of 133.4 mm (5.25") diameter and two facing UV-grade side-mounted slot-shaped quartz windows of 120.7 mm x 12.7 mm (4.75" x 0.50") for laser in/out of the chamber. Critical pressure and temperature of N_2 are 3.4 MPa and 126.2 K and, under

thermodynamic equilibrium, as long as temperature is below the critical temperature it can be considered as liquid. Since liquid phase N_2 injection into the chamber at above the critical pressure is to be attempted, injectant temperature must always be kept below its critical temperature. Also, transport of the liquid through the
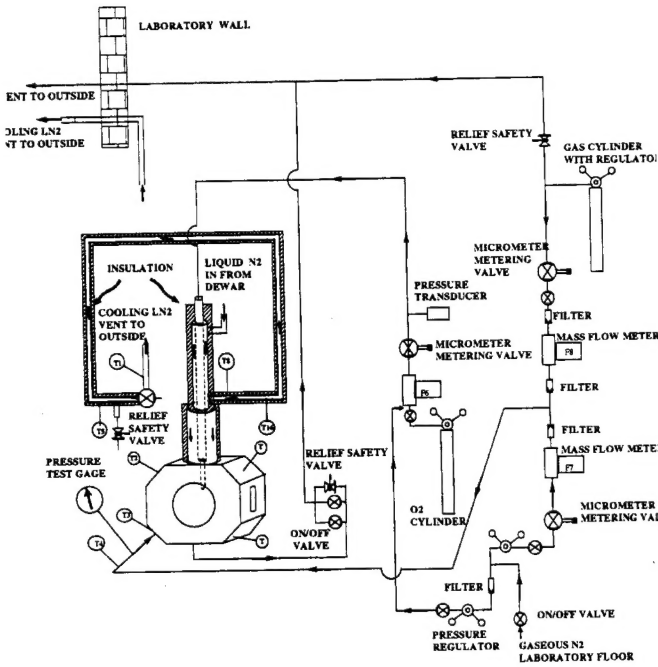
Figure 1. Schematic diagram of experimental setup for sub- to supercritical jet injection.

lines and the injector can be achieved either via application of high pressure inert gas applied into a high pressure cooled N_2 dewar connected to the chamber as in *Mayer et al.[11]*, accepting possibility of dissolved gas; or in our case as shown in Figure 1. The cryogenic cooler uses liquid N_2 from a dewar as the cooling medium. The purpose of this cooler is to cool and/or liquify the injectant passing through it. N_2 from the laboratory is available to be used both as an injectant as well as the chamber medium. Also, a branch is connected for possibility of introduction of other pure or mixture of gases as chamber medium. The mass flow rate of the injectant is regulated and also measured via a mass flowmeter and a precision micrometer valve. For more details refer to *Woodward and Talley [12]*. The injector in this study is a sharp-edged 50-mm long stainless steel tube with 1.59 mm (1/16") diameter and a 254 micron (0.010") inner hole (length-to-diameter ratio of 200). Inlet region for the laminar flow in pipes at Reynolds numbers of 5000 to 10,000 is from 150 to 300 pipe diameters and for turbulent flow from 50 to 100, see *Schlichting [13]*. The length is therefore long enough to ensure fully-developed turbulent pipe flow at the exit.

The experimental rig is fully instrumented with thermocouples, pressure gages and transducers, and mass flowmeters at the locations indicated in Fig. 1. Figure 2

shows details of the image acquisition logical setup along with the timing diagram. The outputs of all measurement devices are connected to a National Instrument AMUX-64T analog multiplexer with special provision for temperature sensor, which itself is connected to a NB-MIO-16X multifunction I/O board (not shown) for Macintosh NuBus computer. A Macintosh computer with a Labview data acquisition software continuously updates all the measured quantities for live inspection and can all be saved with a click of a mouse button. Back-illuminated arrangement is used for initial visual characterization. A QuadTech Stroboslave with a light diffuser in its front provides externally-triggered choices for flash durations
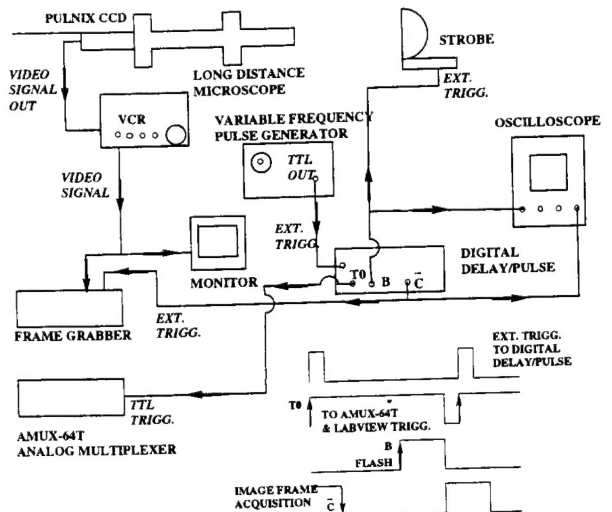
Figure 2. Schematic diagram of the image and data acquisition systems with timing diagram.

of 3, 1.2, and 0.8 microseconds. Almost all the pictures presented in this paper are taken with flash duration of 1.2 microseconds. A model K2 Infinity long-distance microscope with variable focus and manual iris, for illumination and depth of field control, is used to form images of the injected jets presented in this paper. A TM-745E high resolution (768(H) x 493(V) pixels in 8.8(H)x6.6(V) mm actual sensing area) interlaced CCD camera by PULNix with composite video output is used in free run operating mode. The image is captured by a scientific image grabber LG-3 from Scion Corporation installed in another dedicated Macintosh computer and run by the NIH (National Institute of Health) image acquisition and processing software package for Macintosh. Images are analyzed by either ImagePro from Media Cybernatics or NIH image processing software. The pulse command to activate the frame grabber is set to 9.11 ms earlier than the flash timing to ensure capture of the illuminated jets in this free run operating mode. This system provides reliable frame rates of up to 20 frames per second.

Jet structure

Prior to systematic acquisition of images at different conditions, a need for initial evaluation of the system is realized. Specifically, effects of injector mass flow rate and chamber pressure on the injector exit N_2 temperature are investigated. Exit N_2 temperature at the tip of the small injector for this study is measured by installation of an identical tube injector with its hole enlarged only for the last 3 to 4 mm of the length at the exit tip to accommodate a small-sized thermocouple bead without severely obstructing the flow of N_2 through the injector. In this region, a hole is made through the tube's side wall to insert a miniature Omega Type-E 304 SS Sheath Chromega-Constantan exposed-junction thermocouple. A second thermocouple exposed junction is attached to the injector outer wall near the tip and held in contact with the wall by a thick Teflon insulating sheath covering the entire injector tube. These two temperatures are measured simultaneously to document their relationship. The information for the wall temperature alone is then used to estimate the actual tip exit N_2 temperature during all tests, when unmodified injector tube is used. Tests indicates that both thermocouple readings stabilize to different constant values when the injected mass flow rate is above about 125 mg/s. Wall temperature is about 66 +/- 1°C higher than the tip exit value. At a constant mass flow rate, the exit N_2 temperature varies from 99 K to 120 K as relative (chamber) pressure changes from 0.23 to 2.74. This is due to changes in injected N_2 specific heat and density as chamber pressure is varied. In this work, tip temperature is used for calculations of the other jet property values.

To see if effects of buoyancy forces are important within the distances looked in this study, Froude number values are calculated at each chamber pressure. This number changes from 42,000 to 110,000. *Chen and Rodi [14]* propose that the flow is momentum driven as long as a defined nondimensional buoyancy number is less than 0.53 whereas *Papanicolaou and List [15]* suggest this number being less than 1. Considering the more conservative estimate by *Chen and Rodi [14]*, the jet used here is momentum dominated for distances less than 30 to 40 mm from the injector exit. Pictures presented here cover up to about 7 mm (axial distance/diameter ratio of 28) from the injector and hence buoyancy effects can be ignored in favor of the inertia forces.

Figure 3 shows images of the N_2 jet injected into N_2 at a fixed supercritical chamber temperature but varying sub- to supercritical pressure. The iris of the camera and the flash intensity are adjusted to acquire images at the highest contrast possible. A 3.5 mm long real object projects to fill the vertical extent of the images in Fig. 3. Hence, considering 493 pixels in this direction, theoretically, a pixel-to-pixel distance represents 7 micron of real object. On the high resolution prints of the processed images one can recognize objects with real size of about 30 microns and larger. Of course this is an estimate being good by +/- 7 micron band. What we see in these images are demarcation of regions where changes in index of refraction occur due to density variations. At the lowest subcritical chamber pressure in Fig. 3 the jet is liquid-like with surface instabilities that grow downstream where it has twisted appearance. At P_r of 0.43 all instabilities are further amplified until at the next higher pressure where many surface ligaments and drops are seen ejected from the jet. At P_r of 0.83 very fine drops are seen surrounding the jet and its spanwise dimension noticeably grows away from the injector exit plane (i.e., jet diverges). At P_r of 1.03 the N_2 jet enters into a supercritical temperature and pressure environment. There are drastic changes in details of the interface. There are no detectable drops under this condition with the highest software magnification used to view these high resolution images. There are thread- or finger-like entities emerging from the jet which are not broken up into droplets as before but are seemingly dissolved at a spectrum of distance from the dark core. This, in a sense, forms a mixing layer in which phase transition and/or large local density nonuniformities occur. Any further increase of chamber pressure decreases the length and the thickness of the internal dark core and images progressively resemble injection of a gaseous turbulent gas jet into a gaseous environment. Figure 4 is the magnified images of the mixing layer at three subcritical, transitional, and supercritical chamber pressures. Gradual transition from classical liquid-like ligament and drop formations at the interface, seen in liquid atomization regime, to a comb-like structure near the critical point and finally to where submerged turbulent jet appearance emerges can be observed. Inspecting a large set of images at high magnifications, no evidence of drop formation is seen in this gas-like jet regime. These observations are also consistent with images presented by *Mayer et al [11]*. As briefed in the introduction section, the gas-like jet appearance was also proposed by *Newman and Brzustowski [9]* although no high magnification near-injector photographs are shown in their paper. In summary, for N_2 into N_2 injection at the supercritical ambient temperature tested here, there appears to be two structural transitions. One is when the intact jet with irregularly-looking surface waves and downstream shiny twisted-shaped column turns into a somewhat diverging jet with ligaments and many small droplets. The other is when the latter structure changes into a gas-like jet appearance near but below the point where the medium pressure changes from sub- to supercritical conditions (based on the injectant critical pressure). The reason for this behavior, particularly for the change into gas-jet behavior, should be sought in progressive reduction of surface tension and heat of vaporization until they both vanish at and above the critical point. Similar observations are made for the O_2-into-N_2 case but with the transition to gas-like jet at near oxygen critical pressure ($P_r = 0.85$). Observation of the gas-like jet behavior and the lack of any drop formation raises question on relevancy of current injection models and some drop vaporization/combustion results within this regime.

Breakup and atomization regimes of the liquid jet within a narrow chamber-to-density ratio is traditionally shown on a plot of Ohnesorge number versus Reynolds number (Ohnesorge number $= \sqrt{We}/Re$, where We, Weber number, equals to $\rho_l U^2 d/\sigma$, and Reynolds number, Re, is $\rho_l U d/\mu_l$; ρ_l, σ, and μ_l are the liquid density, surface tension, and viscosity respectively; U is liquid exit velocity, and d is the nozzle diameter). On such a plot, in an application where a single liquid is used and surface tension is constant, one moves from left to right on a horizontal line as Reynolds number is increased by changing the injection velocity. Along such a horizontal line and according to *Reitz and Bracco [16]*, one moves from Rayleigh jet breakup to first and second wind-induced breakups and finally to atomization regimes. Rayleigh breakup is caused by the growth of axisymmetric oscillations of the jet surface, induced by surface tension and drop diameters larger than the jet diameter is produced. In the second wind-induced regime, drops are generated by growth of short-wavelength surface waves on the jet surface due to relative motion of the jet and the environment. This unstable growth is opposed by the surface tension, breakup happens at multiple diameter distance, and finally drops with average diameter of less than the jet diameter is produced. In the atomization regime, however, the jet is completely broken up at the nozzle exit and average drop diameter of much less than jet diameter is observed. In Fig. 3, as chamber pressure is increased approaching the critical condition, surface tension is reduced to a near-zero value and for the range of Reynolds number calculated here (25,000 to 75,000) the Ohnesorge number sharply swings from a low (estimated to be 2.8×10^{-3}) to a very large (infinity when surface tension is zero) value. The large Ohnesorge number regime and its importance are indicated in *Faeth [17]* and *Tseng et al. [18]*. The jet under this condition is named "sable jet" for Ohnesorge number values of above 2 to 3 and they state that heavy fuels have higher Ohnesorge number while it becomes large for all liquids at high ambient pressure approaching the critical point due to lowered surface tension. They acknowledge the need for further study in this region. Looking at the regime boundaries proposed by *Reitz and Bracco [16]*, our jet should start in the first and/or second wind-induced zone and quickly pass the atomization regime as chamber pressure is raised from the lowest value shown in Fig. 3. In Fig. 3, one can see first or second wind-induced-like tendencies for the first two lowest chamber pressures, quickly entering into a clear second wind-induced appearance as seen in the next two higher pressure images. However, it seems that before having a chance to show full atomization character, surface tension is sufficiently and rapidly reduced so one achieves gas-like jet appearance near but before reaching the critical pressure value, see Fig. 3. At this condition one sees, in magnified images shown in Fig. 4, that thread-like or finger-like structures are stretched out into the ambient but interestingly appear not broken up into

droplets. As surface tension and heat of vaporization approach near zero values in the vicinity of the critical point, the threads or fingers are gasified and no drops are detected. Transition into full atomization regime is therefore inhibited. Note that the Ohnesorge-versus-Weber number transition criteria do not have gas density or nozzle geometrical effects. Our observed transition inhibition event is therefore tested by another criterion of *Reitz and Bracco [16]* in which chamber-to-injectant density ratio, nozzle geometrical factor, and Weber and Reynolds numbers are all included. Within the limitations of this criteria, no full atomization is allowed. In a sense, as it approaches the critical point, the jet investigated here exhibits a dual character depending on the magnitude of the surface tension and heat of vaporization: liquid-jet like and gas-jet like faces.

Approximate characteristic time estimates also point towards inhibition of the atomization as follows. *Tseng et al. [18]* describe the initial turbulent breakup scenario of the intact jet by formation of a drop from a turbulent eddy with characteristic dimension and cross-stream velocity of "L" and v_L, respectively, in a form of a bulge from the surface of the jet. A characteristic time for the separation of this bulge from the jet to form a drop is proposed to be proportional to $(\rho_l L^3/\sigma)^{1/2}$. On the other hand, vaporization characteristic time of an isolated liquid drop with a diameter of D using the "D-square" law is proportional to D^2/K, where K is the vaporization constant related to the Spalding B-constant by $K = (8k_g/(\rho_l C_{pg}))\ln(B+1)$ and $B = C_{pg}(T_{oo} - T_{boil})/h_{fg}$. Here, k_g, C_{pg} are thermal conductivity and constant-pressure specific heat of the chamber environment gas. The h_{fg} and ρ_l are the density of the liquid drop and latent heat of vaporization at chamber pressure. T_{oo} and T_{boil} are the chamber gas temperature at large distance from the drop and boiling temperature of the liquid substance, respectively. It can be seen that approaching the critical point the σ and h_{fg} decrease to zero and characteristic drop formation becomes very large whereas evaporation time shortens. As indicated in the introduction, the gasification lifetime decreases to a minimum with pressure up to about P_r of 5. Therefore, bulge separation time (to form a drop) is expected to be much larger than the gasification time. Here, the heat up time is neglected as the liquid is near the saturation line. This approximate analysis suggests nonexistence of any drop in the flow field under supercritical condition in an injected liquid jet arrangement. In other words, it will take progressively longer time for the bulges to turn into isolated drops and when/if they do, they are gasified increasingly faster as critical condition is approached. In the limit, although irregularly-shaped jet boundary is formed, they gasify before having the chance to separate into isolated entities.

Jet spreading angle

Looking at images in Fig. 3, one important geometrical parameter that can be quantitatively evaluated is the initial

jet spreading angle or its growth rate. Therefore, this parameter is measured for all acquired images and results along with those of others are presented in Fig. 5. A universal trend can be discovered if nondimensionalized grouping numbers based on appropriate characteristic properties are used to plot the experimental data. As an example see the relevant and excellent work of *Papamoschou and Roshko [1]*. Our initial choice of density ratio in Fig. 5 follows both from liquid spray and gaseous mixing layer works. The angles in our work are measured from the information within a 7-mm distance close to the injector exit face (distance-to-diameter ratio of up to 28). Note that, according to *Abramovich [19]* the length of the potential core in isothermal uniform-density axisymmetric and two-dimensional jets are estimated to be about 16 to 18 injector diameters whereas for nonisothermal cold-into-hot jets it can reach up to about 50 injector diameters. Also, accoring to *Chehroudi et al. [20]* the intact core of the liquid sprays similar to the ones used in diesel engines is $C.d(\rho_l/\rho_g)^{1/2}$ where ρ_l and ρ_g are liquid injectant and chamber gas densities, respectively, d is the effective jet exit diameter and C is a constant between 3.3 to 11. This reflects to an intact core length of between 33 to 110 injector diameters for the chamber-to-injectant density ratio of 0.01 and 16.5 to 55 diameters for the chamber-to-injectant density ratio of 0.04. See Fig. 5 for the range of the density ratio. The foregoing information is to justify that data from corresponding and appropriate initial region is used for growth rate estimations to ensure existence of mixing layer region. At each condition 20 images are used to form an averaged image from which angle measurements are made for presentation in Fig. 5. Both the outer limit and the dark inner core angles are determined by inspection on the computer. A typical example is shown in the inset of Fig. 5. Maximum uncertainty band on angle measurements are also shown for O_2 and N_2 data. Alternatively, the angle for each of the 20 images per condition is measured separately and then averaged. No appreciable differences are observed between the two methods.

Of importance in Fig. 5 are the justification for the selection of the data sets and the nature of their measurements by other researchers. They are elaborated in the following. We consider offering adequate description and review of data by others so that a deeper appreciation of Fig. 5 and its uniqueness can be realized and a reasonable degree of self-sufficiency is achieved. After justification of the selected data and its relation to ours we present our data and offer interpretations. Since the jets investigated here exhibit both liquid-like and gas-like jet appearances, appropriate results for both are discussed here. The simplest is the prediction of the linear jet growth or constant spreading angle for the turbulent incompressible submerged jet. This is derived using the mixing length concept as detailed in the Appendix. Here, the parameter "2b", the jet thickness from the velocity profiles, is apparently measured at the 95% roll-off point. Next, following *Abramovich [19]*, is the semi-empirical equation that attempts to incorporate the effects of

density variations by introduction of a characteristic velocity as shown in the Appendix. See Fig. 5 for the plots of these two cases.

Results of *Brown and Roshko [21]* taken in an experimental setup in which helium and nitrogen are used as the two fluids for their subsonic two-dimensional incompressible turbulent mixing layer studies are important. Note that we also use cooled helium and nitrogen gases in our jet injection study as seen in Fig. 5. They measure mixing layer spreading in a two-dimensional arrangement by both shadowgraphy (called visible jet thickness) as well as through velocity profiles extracted from results of a concentration probe, see *Brown and Rebollo [22]*, along with Pitot tube dynamic pressure measurements within the layer (called vorticity thickness as described in the Appendix). They make distinction between mixing layers in which density changes are caused by temperature changes, high-speed compressible (high Mach number and supersonic) flows, and differences in molecular weights (i.e., different gases). Using forms of the turbulent continuity and momentum equations that are applicable for both the supersonic and incompressible but variable-density cases, they show that if the $\overline{\rho'v'}$ and $\overline{u'v'}$ correlations depend only on density and velocity (and not specifically on temperature or Mach number) then experimental differences between the supersonic and incompressible variable-density mixing layers must be due to differences in other equations to be satisfied for these two cases (i.e., energy equation for the supersonic and mass diffusion equation for the incompressible variable-density cases). Here, the v', u', ρ' are spanwise, streamwise, and density fluctuations with overbar standing for time averaging. The mass diffusion equation leads to $\nabla.U = 0$, a form of the incompressibility statement, in which U is the time-averaged two-dimensional velocity vector. The energy equation for the turbulent supersonic case simplifies to a similar equation but with the left hand side of $P[\nabla.U]$ plus two extra terms. These terms involve the correlation between pressure and transverse velocity fluctuations in one term and pressure gradient across the layer in the other. They state that if these two terms are negligible (i.e., at low Mach number squared values) then there is no distinction between mixing layers made of two streams with differences in molecular weights, differences in temperature, and high speed compressibility effects. This is clear as both equations lead to $\nabla.U = 0$. In the jet we are investigating here there are both differences in temperature as well as molecular weight except for the N_2-into-N_2 case.

For comparison purposes, the two-dimensional turbulent mixing layer experimental data of the *Brown and Roshko [21] is* used to infer the initial spreading rate for axisymmetric jets. Results are plotted in Fig. 5. This is justified since according to both *Brown and Roshko [21]* and *Abramovich et al. [23]*, two-dimensional mixing

layers are found to be fairly well approximated by the initial mixing region of axisymmetric jets. For this reason all angle measurements in our work are made using only the information within the first 7-mm distance of the injector exit plane. We assume a zero value for the ambient velocity (chamber is quiescent in our case), and for this case, there are only two visual growth rates with their corresponding vorticity growth rates reported by *Brown and Roshko [21]*. All other data including the supersonic mixing layer measurements by other researchers (used by *Brown and Roshko* for comparison) are given as vorticity growth rates. Based on these two data points a conversion factor is calculated between the visual and vorticity growth rates. This factor is also applied to the vorticity growth rate values of other researchers collected by and reported in *Brown and Roshko [21]* for the supersonic jets.

Richards and Pitts [24] use a long sharp-edged round tube injecting momentum-dominated helium, propane, and methane turbulent round jets into air. Rayleigh scattering is used to measure concentrations and through concentration plots they define and present a half-radius jet thickness (the radius at which concentration drops by ~~fifty percent~~ 50% of its maximum centerline value). Their first two reported measurement locations, where data for all gases exists, are at distance/radius ratios of 40 and 60 from the injector and are used to calculate the jet spreading angle. Images in Fig. 3 are up to distance/radius ratio of about 55. For this reason we do not use results taken at higher distances for comparison to our data presented in this paper. Based on their mass fraction plots, we judge the full thickness of the jet to be about 4 times the half-radius jet thickness value. This is taken to be the equivalent of the jet visual thickness. Considering that in jets the concentration profiles are generally wider than the velocity profiles, higher values of spreading is expected as shown in Fig. 5.

Papamoschou and Roshko [1] in a series of experiments on sub- to supersonic plane two-dimensional turbulent mixing layers use schlieren photography and Pitot probe (dynamic pressure) to document the mixing layer spreading characteristics. They see, as others in the past, that at supersonic velocities the spreading angle decreases as compared to those of classical turbulent incompressible cases. Although effects of compressibility is at work here but spreading angle also depends on other important parameters such as velocity and density ratios for the two streams forming the mixing layer. Their spreading rate is determined by a linear least square fit to the "Pitot tube thickness" data at distances above 75 mm from a centerbody divider installed in their flow facility. In this work they also discuss the relationship between the three mixing layer thicknesses, namely, δ_{vis} (visual thickness), δ_{pit} (Pitot tube thickness), and δ_{ω} (vorticity thickness). These are defined in the Appendix. They propose the following relationships between them: $\delta_{\omega} = 0.5 \, \delta_{vis}$ and $\delta_{pit} = 1.44 \, \delta_{\omega}$, leading to $\delta_{pit} = 0.72 \delta_{vis}$. However, based

on the data from *Brown and Roshko*, $\delta_{pit} = 0.90 \, \delta_{vis}$ although $\delta_{pit} = 0.80 \, \delta_{vis}$ was finally used following *Konrad [25]*. We use $\delta_{\omega} = 0.5 \, \delta_{vis}$ to convert the supersonic mixing layer results to compare with our visual thickness values.

To separate effects of the compressibility, following *Bogdanoff [26]*, *Papamoschou and Roshko [1]* define a convective velocity (U_c) and a convective Mach number ($M_c = (U - U_c)/a$; a is speed of sound) to be more appropriate than the individual streams' Mach numbers in the mixing layer due to the coherent structures observed by *Brown and Roshko [20]*. It is shown that in a convective system there is a common stagnation saddle point for both streams (first proposed to be considered by *Dimotakis*). At this point, by setting the total pressure expressions the same for the two streams and considering near-equal specific heat ratios one has: $U_c = (\sqrt{\bar{n}_1} U_1 + \sqrt{\bar{n}_2} U_2)/(\sqrt{\bar{n}_1} + \sqrt{\bar{n}_2})$. Where ($\rho_1$, U_1) and (ρ_2, U_2) are density and actual velocity pair of the two streams forming the mixing layer. Note the difference between this equation and the characteristic velocity of equation 5 in the Appendix. For an incompressible variable-density mixing layer, they assume that the main effect of the density ratio is to determine the convective velocity of the structure. And that in a reference frame moving with convection velocity the growth rate is conjectured to be proportional to $\Delta U = U_1 - U_2$. Hence, the density ratio is not in the equation in this moving reference frame and it leads to $\delta_{vis} \sim \Delta U/U_c$. From this, a form of an equation is proposed for the δ'_{vis} (i.e. rate of change of visual thickness in streamwise direction) applicable for incompressible variable-density mixing layers: $\delta'_{vis} = 0.17(\Delta U/U_c) = 0.17(1 - U_2/U_1)[1 + (\rho_2/\rho_1)^{1/2}]/[1 + (U_2/U_1)(\rho_2/\rho_1)^{1/2}]$

The constant 0.17 was obtained experimentally from *Brown and Roshko [21]*. This equation is used to compare with our results and is plotted in Fig. 5 for the U_2/U_1 of zero value. Finally, interesting but not perhaps directly related to our current work, they plot the normalized growth rate of $\delta'_{pit}/\delta'_{pit,0}$ versus the convective Mach number, where $\delta_{pit,0}$ is the Pitot thickness for the incompressible variable-density shear layer having the same density and velocity ratios as the compressible case (i.e., the equation above), and show that all data cluster to form a universal curve. Here, δ_{pit} is the Pitot thickness for the compressible mixing layers at different Mach numbers similar to the ones shown in Fig. 5. Results for different Mach numbers are shown for comparison and completeness only and are not further discussed here. Interested readers should refer to *Papamoschou and Roshko [1]*

Finally, *Dimotakis [2]* uses the observation that, in general, the entrainment into the mixing layer from each stream is not the same and, in a system moving with the

8

aforementioned convection velocity, offers a geometrical argument to derive an equation for the two-dimensional incompressible variable-density vorticity thickness growth of the form

$$\delta_\omega' = \varepsilon\{(1 - U_2/U_1)/[1 + (\rho_2/\rho_1)^{1/2}(U_2/U_1)]\}\{1 + (\rho_2/\rho_1)^{1/2}$$
$$- [1 - (\rho_2/\rho_1)^{1/2}]/[1 + 2.9(1 + U_2/U_1)/(1 - U_2/U_1)]\}$$

This growth rate is multiplied by a factor of 2 to convert to visual shear layer thickness growth rate and is plotted in Fig. 5 for ε value of 0.17/2 after adaptation to the axisymmetric jets. In Fig. 5 this equation intersects the one by *Papamoschou and Roshko [1]* at density ratio of 1 and they gradually depart on either sides.

Since images in Fig. 3 show both liquid-like and gas-like visual jet appearances, it makes sense and is appropriate to also show the spreading angle for liquid sprays produced from single-hole nozzles typical of the ones used in diesel engines. The atomization of liquids is a complex phenomenon that depends on many parameters among them are: injector geometry, ambient density, viscosity and surface tension of the liquid, initial turbulence, cavitation, and liquid supply pressure oscillations. According to *Reitz and Bracco [16]*, visually, in "full" or simply atomization regime the liquid jet diverges at the exit of the injector hole. Also, using aerodynamic surface wave growth mechanism for liquid atomization they show that the spray angle can be determined by combining the radial velocity of the fastest growing unstable surface waves with the axial injection velocity. A form of an equation is then derived for the spray spreading angle that reproduces the experimental trends of square root of the ambient-to-injectant density ratio as well as the viscosity dependencies. They indicate that the incompressible variable-density equation proposed in *Abramovich [19]* significantly overpredicts the spray spreading angle for all nozzles at low chamber gas densities (this equation is derived by setting the U_r to zero in equation 6 of the Appendix). This can be seen in Fig. 5. The spray angle in the atomization regime is measured using information within the first 5 mm distance from the nozzle exit plane (distance-to-diameter ratio ranging from 20 to 40). Therefore, the measurements are within the comparable spatial region where we measure our spreading rates. For the two cases shown in Fig. 5 the Reynolds number range between 25,000 to 40,000. For any given nozzle with fixed length-to-diameter ratio the spray angle widens appreciably beyond the Reynolds number values of about 25,000. Both *Reitz and Bracco [16]* and *Hiroyasu and Arai [27]* show profound effects of the nozzle design on the spray angle. Therefore, equations proposed by *Reitz and Bracco [16]* for two different length-to-diameter ratios along with their corresponding vertical bar-bands indicating experimental scatter around them are shown in Fig. 5. Experimental data are taken for the isothermal sprays. As a cross check, recent curve-fitted equation to experimental data proposed by *Naber and Siebers [28]* is also shown. They use transient liquid fuel jet into a high pressure chamber for both nonvaporizing and vaporizing sprays. Their

angle measurement zone extends beyond our initial region and this to some extent contributes to disagreement seen between the two sets of data for liquid sprays at injector length-to-diameter density ratio of about 4, see Fig. 5. Their vaporizing liquid spray data show 15% reduction in spreading angle at density ratio of 0.01 decreasing to no noticeable reduction at the ratio of 0.04. This is explained to be due to contraction of the jet caused by the entrained ambient gas cooled by the vaporizing liquid as well as the vaporization of the drops at the outer boundary of the spray. This is important and suggests that the vaporizing versions of the isothermal sprays in Fig. 5 are not much different from the ones shown therein.

The choices of the axes in Fig. 5 are affected by the form of the theoretical equations proposed by *Reitz and Bracco [16]* and *Papamoschou and Roshko [1]* as discussed above. This figure covers a density ratio of a 1000 from liquid sprays to supersonic mixing layers, a unique and new plot on its own. Unfortunately, data presented in this figure does not cluster to form a universal curve and as such choices of the normalized axes are incomplete. This is not surprising in light of the proposal by *Papamoschou and Roshko [1]* in relation to their mixing layer data mentioned earlier. Clearly, within the range plotted, the results of constant spreading angle of incompressible turbulent jet overpredicts nearly all others in Fig. 5. There are also increasing disagreement between turbulent gas jet of *Abramovich [19]* and incompressible variable-density model of *Papamoschou and Roshko [1]* as density ratio increases. Within the range shown, axisymmetric jet spreading angle by *Richards and Pitts [24]* is higher in value than all others due to the reason mentioned earlier. Supersonic jet angle narrows as density ratio is decreased (or Mach number increased). To some extent, for measured values, disagreements in this figure can be attributed to different definitions of the mixing layer thicknesses and their measurement methods. In a sense, data in Fig. 5 is visual thicknesses and not always they are measured directly, hence conversion from vorticity and/or Pitot thicknesses are required. We have used the best estimates of this conversion factor based on works of others as described earlier. Even for those cases where visual thicknesses are measured directly, different photographic techniques are employed causing a certain yet-to-be-assessed degree of variability between different researchers.

For the N_2-into-N_2 case tested in this work, an average curve (not drawn) through the data points in Fig. 5 intersects the *Papamoschou and Roshko [1]* curve somewhere at the density ratio of 0.09. This can be closely observed in the inset in Fig. 5. Departure between the two increases below the critical pressure of N_2 where the jet appears liquid-like, going even below the *Dimotakis's* equation, see Fig. 3 and 5. Note that the tendency of our data to approach those of liquid sprays generated by a comparable high length-to-diameter ratio nozzle (i.e., 85) is evident. Data for O_2-into-N_2 case shows a steeper drop in angle near but below its own

critical pressure in Fig. 5. To build confidence and also generate gaseous jet data using the identical arrangement employed by us to acquire the sub- to supercritical jet images, we injected cooled He gas into the N_2 chamber and vice versa. Results are shown in Fig. 5 for a range of chamber pressures from 0.77 to 9.19 MPa. Although there is scatter in the data at various chamber pressures, it is interesting that the narrowing of the angle is seen as injection of the cooled N_2 into He is considered, consistent with the *Brown and Roshko's* data. The shift to lower density ratios seen in our data is because the injectants are cooled. Injection of N_2 into mixtures of N_2+CO is also considered. In general, effects of these mixtures are through the changes they cause in chamber-to-injectant density ratio, surface tension, and diffusion of N_2 into the ambient. In a binary mixture, we speak of critical "mixing" condition. The case of CO is interesting as its critical pressure and temperature (3.494 MPa, 132.82 K) are very close to those of N_2, so critical mixing condition should be near the pure N_2 case, and has the same molecular weight and specific heat values. Hence, addition of any fraction of CO to N_2 should not change the density ratio, critical condition, and thermal properties. The only relevant property expected to change is the surface tension and its effects should be felt in structural transitions discussed earlier. A more comprehensive discussion of these results should await completion of all the scheduled experiments. However, the spreading rate measurements of the N_2 into N_2+CO mixture closely follows the *Papamoschou and Roshko [1]* theoretical curve increasing the confidence level on our measurements.

It is clear that for a range of density ratios in which our images show gas-jet like appearance the experimental data agrees well with the proposed theoretical equation by *Papamoschou and Roshko [1]* and closely follows the trend of *Dimotakis [2]*. This can be taken as further and quantitative confirmation that at ambient supercritical pressure and temperature conditions (based on the injectant values) the injected jets visually behave like a gas though technically it may be referred to as "fluid". It is interesting that results for the liquid sprays tend to converge to incompressible jet value at high density ratios for the short length-to-diameter nozzle and not the proposed *Papamoschou and Roshko [1]* equation. There is marked disagreement in both magnitude and slope between liquid sprays (at a comparable length-to-diameter ratio of 85) and our data, see Fig. 5, even though the jet investigated here appears to go through initial phases of the liquid atomization process, see Figs. 3. One expects that our jet should follow the liquid spray results but it does not. Also, pure evaporation of the liquid sprays should narrow the spreading angle as shown by *Naber and Siebers [28]* making this disagreement even farther. The reason is that although the jet studied here shows second wind-induced breakup features similar to liquid jets, it fails to reach full atomization state as chamber pressure (really density) is raised. This is because the thermodynamic state approaches the critical point and

consequently both surface tension and heat of vaporization are reduced to a near zero value. Transition into the full atomization region is therefore inhibited.

Therefore, all evidences presented here point towards a gas-jet like behavior within the indicated region. They are: (1) lack of droplet visual detection in the acquired images (smallest detectable is about 30 microns) and visual impression of a gaseous jet; (2) inhibition of transition into the full atomization zone due to lowered surface tension tested by the available atomization criteria; (3) rapid gasification due to vanishingly small heat of vaporization; and (4) agreement of the jet spreading rate measurements with those of incompressible but variable-density gas jets theory (5) disagreement of the liquid spray spreading rate data with comparable nozzle geometry. Although strictly speaking droplets less than about 30 microns cannot be definitively judged by the imaging system employed here, all aforementioned evidences tend to strengthen our gas-jet like picture of the investigated jet near and above the critical point of the injectant. A search for a universal curve to cover all the data in Fig. 5 is a challenging one. To date, no appropriate nondimensionalized parameters are found to collapse all spreading rate information on a single curve. Appropriateness of the surface tension for liquid jets and sprays and its irrelevance for gaseous jets are among the issues to be reconciled.

Summary and conclusions

Structural transition and spreading angle (or growth rate) of jets injected into an environment at fixed supercritical temperature but varying pressure from sub- to supercritical are analyzed. N_2, O_2, and He are injected into N_2, He, and mixtures of CO+N_2 at different proportions. Increasing chamber pressure from a low subcritical value, the fluid in the jet appears to go through classical liquid jet breakup stages up to a second wind-induced breakup regime. In this regime one sees a divergent jet with ligaments and many droplets ejecting from the jet. Penetration into the full atomization regime is inhibited near but before the critical pressure of the injectant because of the combined effects of lowered surface tension and heat of vaporization. At this point the jet assumes a gas-jet like appearance that remains up to the highest pressure tested here. Also, a unique and new plot is formed by converting all other types of spreading rates to the visual growth rate using most relevant works of others on variable density incompressible mixing layers, axisymmetric incompressible and compressible gas jets, supersonic jets/mixing layers, and liquid sprays, covering an ambient-to-injectant density ratio range of a 1000. Spreading angle of the jets in our work is measured from a large set of images and compared with all the aforementioned data by others. Results clearly follow a theoretical equation proposed by *Papamoschou and Roshko [1]* for an incompressible but variable density turbulent mixing layers. This agreement for spreading angles starts at a pressure near but below the

thermodynamic critical value of the injectant substance, quantitatively confirming gas-jet like visual appearance observed in images of the jets for the first time. This jet, therefore, exhibits a dual character behavior: a liquid-jet like and gas-jet like faces depending on the values of surface tension and heat of vaporization. Therefore, (1) inability of droplet visual detection in the acquired images and their visual impression of a gaseous jet, (2) inhibition of transition into the full atomization zone due to lowered surface tension tested by the available atomization criteria, (3) rapid gasification due to vanishingly small heat of vaporization, and (4) agreement of the jet spreading rate experimental measurements with those of incompressible but variable density gas mixing layers theory, (5) disagreement with the liquid spray spreading rate data, all tend to strengthen the position that at near and above the critical point of the injectant the jet exhibits gas-jet like behavior. Considering this, relevancy of current injection models and some drop vaporization/combustion results under the conditions where gas-jet like behavior is detected should be reexamined.

Acknowledgement

References

1. Papamoschou, D. and Roshko, A.. "The compressible turbulent shear layer: an experimental study," J. Fluid Mech., vol. 197, 1988, pp. 453-477.

2. Dimotakis, P. E. "Two-dimensional shear-layer entrainment," AIAA Journal, 21, No. 11, 1986, pp. 1791-1796.

3. Bruno, T. J. and Ely, J. F. *Supercritical fluid technology: review in modern theory and applications*, CRC Press, 1991.

4. Lazar R. S. and Faeth, G. M. "Bipropellant droplet combustion in the vicinity of the critical point", Thirteen Symposium (International) on Combustion, The Combustion Institute, P.801, 1971.

5. Umemura, A. "Supercritical droplet gasification combustion," IUTAM Symposium on theories ? combustion on droplets and sprays, December 1994, Taiwan.

6. Givler, S. D. and Abraham, J. "Supercritical droplet vaporization and combustion studies," Prog. Energy Combust. Sci. vol. 22, 1996, pp. 1-28.

7. Faeth, G. F., Dominicis, D. P., Tulpinsky, J. F., and Olson, D. R. Supercritical bipropellant droplet combustion," Twelfth Symposium (International) on Combustion, The Combustion Institute, 1969, P. 9.

8. Shuen, J. S., Yang, V., and Hsiao, C. C. "Combustion of liquid fuel droplets in supercritical conditions," Combustion and Flame, 89, 1992, pp. 299-319.

9. Newman, J. A. and Brzustowski. "Behavior of a liquid jet near the thermodynamic critical region," AIAA Journal, vol. 9, 1971, no. 8, pp. 1595-1602.

10. Mayer, W., Schik, A., Schweitzer, C., and Schaffler, M. "Injection and mixing processes in high pressure LOX/GH2 rocket combustors," AIAA Paper no. 96-2620, 32nd AIAA/ASME/SAE/ASEE Joint Propulsion Conference & Exhibit, Lake Buena Vista, Florida, 1996.

11. Mayer, W., Ivancic, A., Schik, A., and Hornung, U. "Propellant atomization in LOX/GH2 rocket combustors," AIAA Paper no. 98-3685, 34 th AIAA/ASME/SAE/ASEE Joint Propulsion Conference & Exhibit, Cleveland, Ohio, July 13-15, 1998.

12. Woodward, R. D. and Talley, D. G. "Raman imaging of transcritical cryogenic propellants," AIAA Paper 96-0468, 34 the AIAA Aerospace Sciences Meeting and Exhibit, Reno, Nevada, January 1996.

13. Schlichting, H. *Boundary Layer Theory*, MacGraw-Hill Book Company, seventh edition, 1979.

14. Chen, C. J. and Rodi, W. "Vertical Turbulent Buoyant Jets- A Review of Experimental Data. 1980, Pergamon.

15. Papanicolaou, P. N. and List, E. J. "Investigations of round vertical turbulent buoyant jets," J. Fluid Mech., 195, 1988, pp. 341-391.

16. Reitz, R. D. and Bracco, F. V. "On the dependence of spray angle and other spray parameters on nozzle design and operating condition," SAE international Congress and Exposition, SAE Paper no. 790494, Detroit, Michigan, February 26-March 2, 1979.

17. Faeth, G. M., "Structure and atomization properties of dense turbulent sprays," Twenty-third Symposium (International) on Combustion, The Combustion Institute, P.1345, 1990.

18. Tseng, L.,-K., Ruff, G. A., P.-K., Wu, Faeth, G. M., "Continuous- and dispursed-phase structure of pressure-atomized sprays," Progress in Astronautics and Aeronautics: Recent Advances in Spray Combustion, February, 1995.

19. Abramovich, G. N. *The theory of turbulent jets*, M.I.T. Press, 1963.

20. Chehroudi, B., Chen, S. H., Bracco, F. V., and Onuma, Y. "On the Intact Core of Full-Cone Sprays," Society of Automotive Engineers, 1985 Congress and Exposition, SAE Transaction Paper 850126, February 25-March 1, 1995.

21. Brown, G. and Roshko, A. "On density effects and large structure in turbulent mixing layers," J. Fluid Mech., vol. 64, 1974, part 4, pp. 775-816.

22. Brown G L, and Rebollo, M R, "A small fast-response probe to measure composition of a binary gas mixture," AIAA Journal, 10, 1972, 649.

23. Abramovich, G. N., Yakovlevsky, O. V., Smirnova, I. P., Secundov, A. N., and Krasheninnkov, S., Yu. "An Investigation of turbulent jets of different gases in a general stream," Astronautica Acta, 14, 1969, 229.

24. Richards, C. D. and Pitts, W. M. "Global density effects on the self-preservation behavior of turbulent free jets," J. Fluid Mech., vol. 254, 1993, pp. 417-435.

25. Konard, J. H. "An experimental investigation of mixing in two-dimensional turbulent shear flows with applications to diffusion-limited chemical reactions," PhD thesis, California Institute of Technology, 1976.

26. Bogdanoff, D. W. "Compressibility effects in turbulent shear layers," AIAA Journal, 21, 1983, pp. 926-927.

27. Hiroyasu, H. and Arai, M. "Fuel spray penetration and spray angle in diesel engines," Trans. JSAE, Vol. 21, 1980, pp. 5-11.

28. Naber, J. D. and Siebers, D. L. "Effects of gas density and vaporization on penetration and dispersion of diesel sprays," SAE international Congress and Exposition, SAE Paper no. 960034, Detroit, Michigan, February 26-29, 1996.

Appendix

(a) Growth rate for the incompressible and compressible jets are documented in *Abramovich [19]*:

For an incompressible turbulent submerged jet three special regions are defined: initial, transitional, and main regions. Initial region roughly extends just beyond the end of the potential core and the main region is where strictly self-similarity solution becomes applicable. Using Prandtel's mixing length theory, assuming mixing length being only function of streamwise distance, *Abramovich [19]* indicates that the jet growth rate is controlled by the transverse velocity fluctuations, v':

$$\frac{Db}{Dt} \propto v' \propto -\ell \frac{\partial U}{\partial y} \propto -\ell \frac{U_{cl}}{b} \propto U_{cl} \qquad (1)$$

and since

$$\frac{Db}{Dt} = \frac{db}{dx}\frac{dx}{dt} \propto U_{cl}\frac{db}{dx} \qquad (2)$$

from the above two :

$$\frac{db}{dx} = \text{constant} \Rightarrow b = (\text{constant})x \Rightarrow$$

$$\ell = (\text{constant})\, x \qquad (3)$$

2b is defined as the thickness of the velocity profile, Db/Dt is the total derivative, ℓ is mixing length, v' is the transverse velocity fluctuations, and U_{cl} is the centerline maximum value of the time-averaged streamwise velocity profile.

Abramovich [19] in a semi-empirical theory proposes an equation for the jet spreading considering compressibility as follows:

$$\frac{db}{dx} \propto \frac{U_1 - U_2}{U_{char}}; \text{ where } U_1 \text{ and } U_2 \text{ are streamwise}$$

velocities at the boundaries of the mixing zone, U_{char} a characteristic velocity in the zone, and x is in streamwise direction.

For incompressible flow : $U_{char} = \dfrac{U_1 + U_2}{2}$ (4)

For compressible flow : $U_{char} = \dfrac{\rho_1 U_1 + \rho_2 U_2}{\rho_1 + \rho_2}$ (5)

In the main region of the jet :

$$U_r = \frac{U_{ambient}}{U_{cl}};$$

$$\rho_r = \frac{\rho_{ambient}}{\rho_{cl}}; U_{cl} = U_{cl}(x); \rho_{cl} = \rho_{cl}(x)$$

If U_r and ρ_r do not depend on x then from above :

$$\frac{b}{x} = C\frac{1 + \rho_r}{2}\frac{1 - U_r}{1 + \rho_r U_r} \qquad (6).$$

From experiments in the initial region of the submerged jet (i.e., $U_r = 0$) of an incompressible fluid ($\rho_r = 1$) C = 0.27

is proposed. However, various experiments in hot jets, high - velocity jets, and supersonic jets under off - design discharge suggest a value of $C = 0.22$.

From above equations for compressible flow :

$$\frac{db}{dx} = C \frac{1 + \rho_r}{2} \frac{1 - U_r}{1 + \rho_r U_r}; \text{ where}$$

$$U_r = \frac{U_2}{U_1} \text{ and } \rho_r = \frac{\rho_2}{\rho_1}.$$

(b) Definition of different mixing layer thicknesses:

Vorticity thickness: δ_ω is defined through measurements of the streamwise time-averaged (U) velocity profile in the mixing layer. It is equal to $(U_1 - U_2)/ (dU/ dy)_{max}$ where derivative is taken across the mixing layer and U_1 and U_2 are the free stream velocities for each stream forming the mixing layer. *Brown and Roshko [21]* state that this definition in addition to being convenient is also appropriate. The problem of the growth of the turbulent mixing layer being basically the kinematic problem of the unstable motion induced by the vorticity.

Pitot thickness: δ_{pit} is the width of the Pitot-tube-measured pressure profile from 5% to 95% of the difference of the two free-stream values, see *Papamoschou and Roshko [1]*.

Visual thickness: δ_{vis} is the thickness determined via a photographic technique. It is measured by shadowgraphy and schlieren approaches in *Brown and Roshko[21]* and *Papamoschou and Roshko [1]*, respectively.

Nomenclature

b	:Velocity profile half thickness
C_{pg}	:Constant pressure specific heat for the gas
d	:Injector tube diameter
D	:Drop diameter
F_r	:Froud number
h_{fg}	:Heat of vaporization
k_g	:Thermal conductivity of the gas
ℓ	:Prantdel's mixing length
L	:Characteristic dimension of turbulent eddies
M_c	:Convective Mach number
Oh	:Ohnesorge number
P_c	:Critical pressure of the injectant
P_{ch}	:Chamber pressure
P_r	:P/P_c
R_e	:Reynolds number
T_r	:T/T_c
T_{ch}	:Chamber temperature
T_{00}	:Environment temperature at a large distance from the surface of the drop
T_{boil}	:Boiling point temperature

|	
u'	:Streamwise velocity fluctuations
U_1	:Free stream velocity of the high-velocity stream in the mixing layer
U_2	:Free stream velocity of the low-velocity stream in the mixing layer
U_c	:Convection velocity
U_{cl}	:Jet centerline velocity
U_r	:U_2/U_1
v'	:Spanwise velocity fluctuations
v_L	:Cross stream velocity over a separating bulge from the interface of the liquid jet
W_e	:Weber number
ρ_l	:Liquid density
ρ_g	:Gas density
ρ'	:Density fluctuations
ρ_1	:Free stream density of the low-velocity stream in the mixing layer
ρ_2	:Free stream density of the high-velocity stream in the mixing layer
ρ_r	:ρ_2/ρ_1
σ	:Surface tension
δ_{vis}	:Visual mixing layer thickness. See Appendix
δ_{pit}	:Pitot-tube mixing layer thickness. See Appendix
δ_ω	:Vorticity thickness. See Appendix
δ'	:Spatial rate of change of the thickness or spreading rate
$\delta_{pit,0}$	:Pitot thickness for the incompressible variable-density shear layer having the same density and velocity ratios as the compressible case
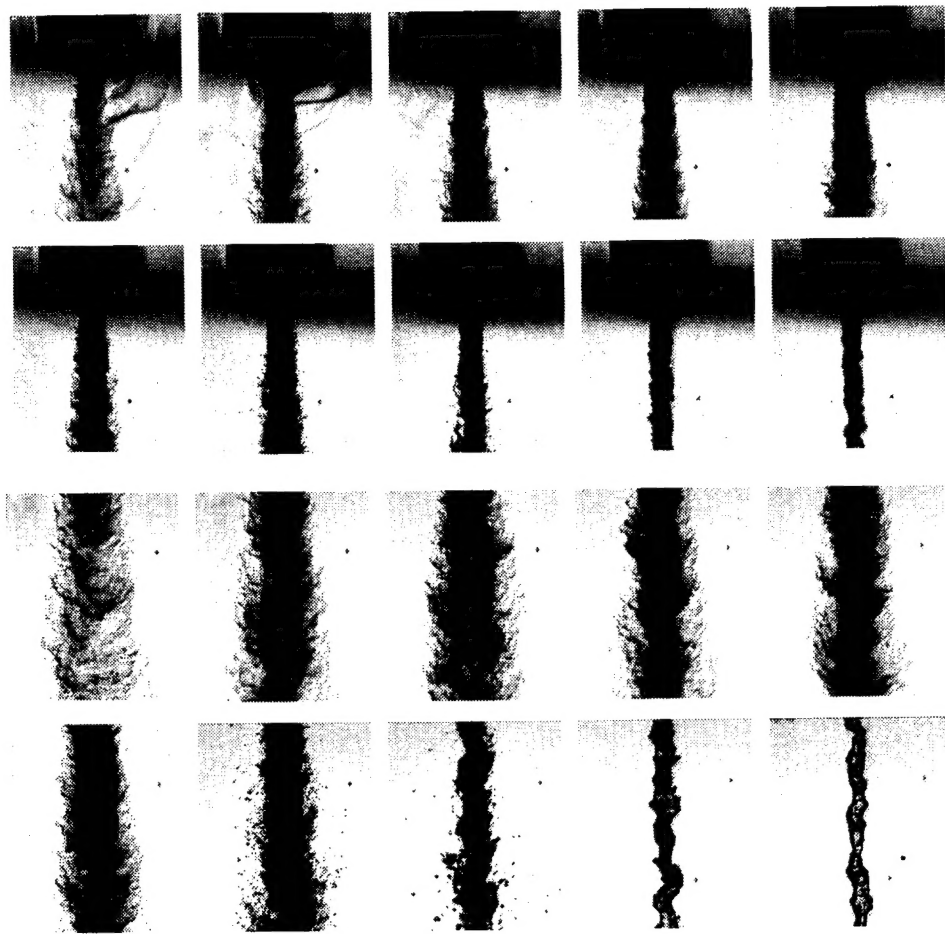
Figure 3. Back-illuminated images of the nitrogen injected into a chamber of nitrogen at a fixed supercritical temperature of 300 K but varying sub- to supercritical pressure. For the first two rows, chamber pressure decreases left to right from upper-left to lower-right corner: P_{ch}/P_c= 2.74, 2.44, 2.03, 1.64, 1.23, 1.03, 0.83, 0.63, 0.43, and 0.23. Lower two row images are corresponding images for the upper ones but further downstream. The axial distance at the bottom of the upper two row images is the same as the top of the ones in the two lower rows. The magnification can be inferred knowing the injector outer diameter of 1.59 mm (1/16"). Re # range: 25,000 to 75,000; injection velocity range: 10 to 15 m/s; Froude # range: 40,000 to 110,000. P_c and T_c are critical pressure and temperature of the injectant and P_{ch} and T_{ch} are chamber pressure and temperature. For N_2: P_c=3.4 MPa, T_c=126.2 K.

Pch=3.13 MPa
Reynolds=75,281
Mass flow=352 mg/s
Inj. Velocity=14.9 m/s

Pch=4.14 MPa
Reynolds=66,609
Mass flow=350 mg/s
Inj. Velocity=14.1 m/s

Pch=9.19 MPa
Reynolds=42,830
Mass flow=350 mg/s
Inj. Velocity=11.7 m/s

Appearance of conventional breakup of liquid surface indicating ligaments and drops ejecting from the mixing zone

Mixing layer affected by sub- to supercritical transition. No drops are seen

Appearance of Gas/gas mixing layer

Figure 4. Software magnified images of the jet at its outer boundary showing transition to the gas-jet like appearance starting at just below the critical pressure of the injectant. Images are at fixed supercritical chamber temperature of 300 K.
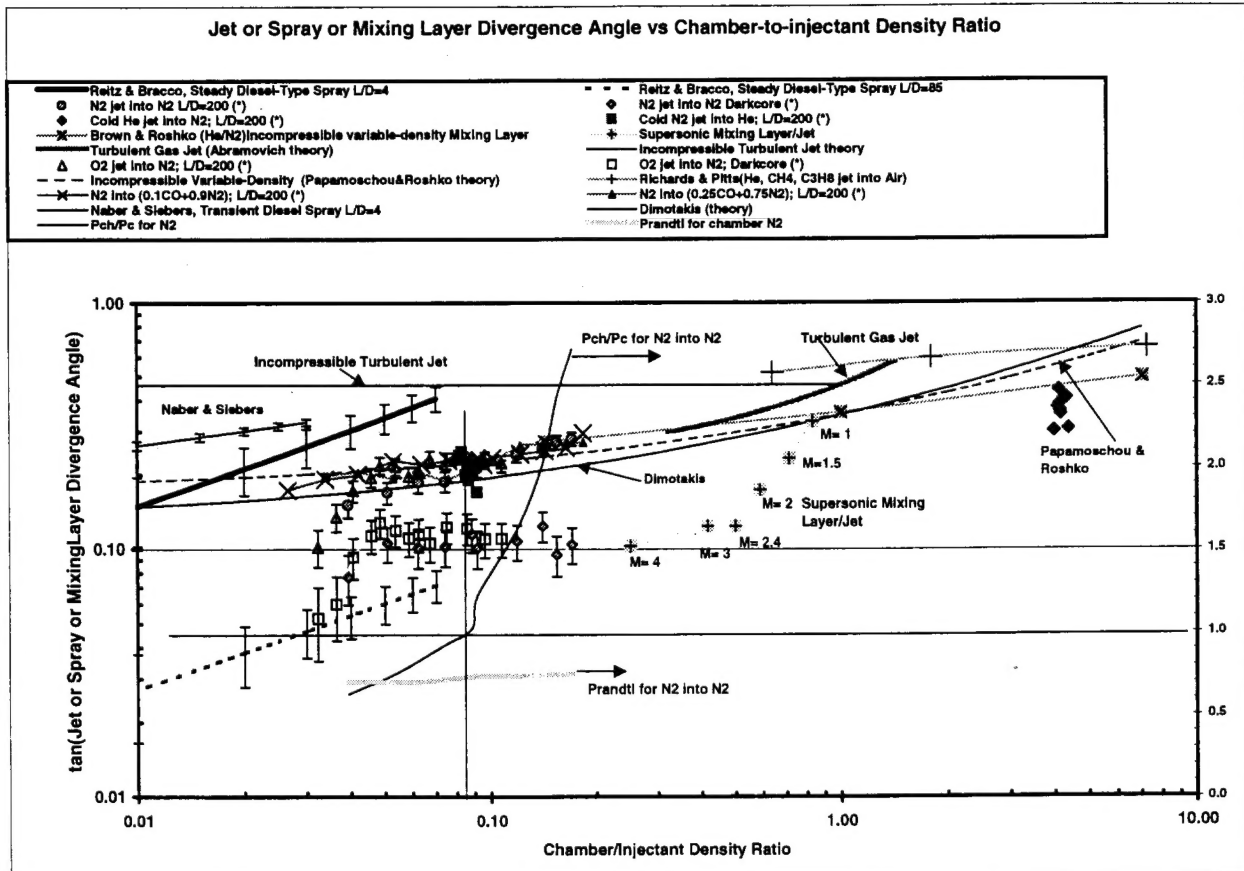
Figure 5. Shows spreading or growth rate as tangent of the visual spreading angle versus the chamber-to-injectant density ratio. (*) refers to data taken at AFRL.